

# Nucleation Rate Surface Topologies for Binary Systems<sup>†</sup>

Michael P. Anisimov and Philip K. Hopke\*

Department of Chemical Engineering, Clarkson University, Potsdam, New York 13699-5707

Received: May 14, 2001; In Final Form: June 25, 2001

Recent experiments have found that two nucleation rate surfaces can be observed for two different critical embryo phases (solid and liquid) near the triple point of the condensing species. Direct experimental evidence was presented of the existence of two independent nucleation rate surfaces with one of them existed over metastable vapor–liquid-phase equilibrium lines. These results force more careful consideration of the role of metastable phase equilibria in the topology of nucleation rate surfaces. In the present study, the topology of the nucleation rate surface for a binary vapor in which partial solubility of the condensed components is considered. Schematic multiple surfaces over the phase diagram with a eutectic point, presenting two-channel nucleation, are constructed. Vapor–liquid nucleation in a carrier gas in most cases is a binary system with partial solubility of condensate. It is reasonable to propose that multiple nucleation rate surfaces are common phenomena for many systems. Sulfur hexafluoride–*n*-pentanol nucleation was experimentally studied using a flow diffusion chamber. The experimental results for *n*-pentanol–sulfur hexafluoride at total pressures of 0.10, 0.20, and 0.30 MPa are presented. All experimental conditions were recalculated to correspond to a nucleation temperature of 255.0 K. The observed convoluted lines of  $\ln J$  plotted against  $\ln S$  provide experimental evidence of the existence of multiple nucleation rate surfaces. It can be anticipated that a variety of multiple nucleation rate surfaces, such as presented here, will be detected soon. Obviously, the application of one-component nucleation theory for such systems with multiple nucleation rate surfaces will not be consistent with the data. Separation of the multiple nucleation surfaces reduces the problem to a simpler one-channel treatment of nucleation. It will then be possible to construct a consistent nucleation theory for a given series of compounds.

## Introduction

Homogeneous vapor nucleation theory has been developing from the time of Willard Gibbs. Around 50 years ago, the first stage of formal nucleation theory was developed and has come to be termed classical nucleation theory (CNT). This theory is applicable to a broad spectrum of first order phase transitions. The CNT modifications are used to describe melting, freezing, boiling, condensation, sublimation etc. The CNT has been most frequently used for the case of vapor–liquid nucleation where experimental measurements have the most progress.

However, there are those, for example, Senger et al.,<sup>1</sup> who think that one universal nucleation theory is not available now, but that multiple nucleation theories can be constructed for each separate series of reduced systems. Indeed, the simplest consideration of the recent idea by Anisimov et al.,<sup>2</sup> that nucleation rate surfaces originate from lines of the phase equilibria, does not lead to a universal nucleation theory that could be created until a universal, nonparametric theory of the phase equilibrium diagrams is available. The number of the irreducible phase equilibrium diagrams is substantial. This result suggests that now many theories of nucleation can be constructed for many series of single or multiple component systems, i.e., at least one theory for each series with the similar (reducible) phase state diagrams.

Recently, Anisimova et al.<sup>3</sup> experimentally determined that in the vicinity of the triple point, two nucleation rate surfaces

can be observed for two different phases (solid and liquid) of the critical embryos. More importantly, these authors<sup>3</sup> found direct experimental evidence of the existence of two independent nucleation rate surfaces such that one of them is constructed over the metastable vapor–liquid-phase equilibrium lines. In the present research, the topology of the nucleation rate surface for a binary vapor system with partial solubility of the condensed components is studied.

## Two Channel Nucleation

Using semiempirical construction of nucleation rate surfaces,<sup>2</sup> it was shown that for phase transitions of the first order, nucleation rate surfaces for each of the two different phases that may exist in the critical embryos produced near the triple point can be constructed. Following this result, Anisimova et al.<sup>3</sup> have shown that simple measurements of the aerosol size distribution at nucleation temperatures near the triple point of the condensing material permit the observation of nucleated particles produced through two different nucleation channels. Indeed, because of the molecule accommodation difference, the growth rate of clusters with differing phases should be different and can result in the production of different sized particles for each of the different phases in the clusters. More importantly, these authors<sup>3</sup> found direct experimental evidence of the existence of two independent nucleation rate surfaces such that one of them has to be constructed over the metastable vapor–liquid-phase equilibrium lines.

In Figure 1a, two nucleation rate surfaces can be observed in the vicinity of the triple point.<sup>2</sup> Schematically, nucleation at

<sup>†</sup> Part of the special issue "Howard Reiss Festschrift".

\* To whom correspondences should be addressed. E-mail: hopkepk@clarkson.edu.

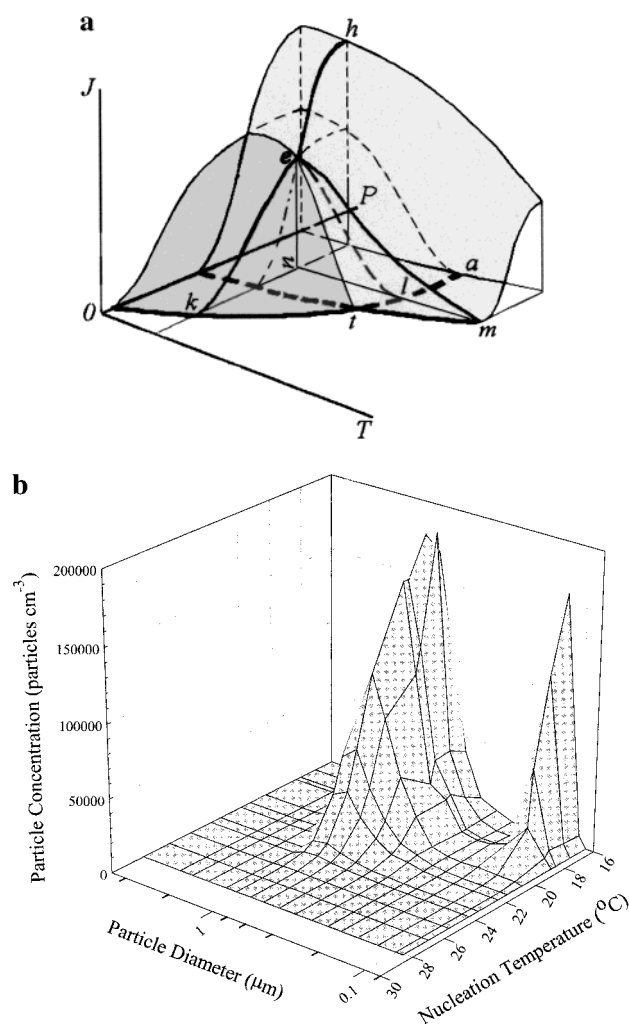


**Figure 1.** (a) Two nucleation rate surfaces in the vicinity of the triple point,  $t$ . Schematically, the higher temperature nucleation, for example, droplets at constant pressure, is shown by line  $em$ . The dashed line,  $el$ , depicts the lower temperature (crystal) nucleation rate. The temperature lowering from point  $m$  at constant pressure leads the droplet formation and then (at point  $l$  and lower) both droplet and crystal nucleation. (b) The experimental result<sup>3</sup> illustrates clear bimodal size distribution.

higher temperature produces a single phase. For example liquid phase (droplet) nucleation at constant pressure is shown by line  $em$ . The dashed line,  $el$ , depicts the lower temperature (crystal) phase nucleation rate. Lowering the temperature from point  $m$  at constant pressure leads to droplet formation and then at point  $l$  and lower, both droplet and crystal nucleation can occur. The experimental result<sup>3</sup> in Figure 1b illustrates clearly bimodal size distributions. It is assumed that droplets produce the larger sized particles with the wider distribution, while the smaller peak reflects the crystal particle formation. Only droplets are produced at a sufficiently high nucleation temperature, which is consistent with the nucleation rate surface topology, depicted in Figure 1a. The result by Anisimova et al.<sup>3</sup> provides the basis for interpreting nucleation of two concurrent (stable and metastable) phase states of critical embryos, for example, by Anisimov et al.<sup>4,5</sup> or by Strey and Wagner<sup>6</sup> as two-channel nucleation near the conditions of a phase transition.

The experimental system in which size distribution measurements are made has good possibilities for discerning aerosol particles produced through two channels such that nucleation rates can be measured for each channel. It is then possible to

use the slopes of the nucleation rate surfaces to estimate the number of critical embryo molecules in the one channel approximation. To explore these concepts further, the conceptual framework for nucleation rate surface construction will be presented followed by a description of the experiments on the *n*-pentanol–sulfur hexafluoride system.

### Vapor Nucleation Surface

**Fully Miscible System.** The nucleation rate surface for a binary system with partially miscible components in condensed state can be constructed over an isothermal  $P$ – $X$  phase diagram, where  $P$  is the total pressure and  $X$  is the composition. Following the approach of Anisimov et al.,<sup>2</sup> the surface will be discussed in terms of steady-state nucleation rates. To design the surfaces of nucleation rates, the following assumptions are used:

(1) A given phase can exist beyond its interface equilibrium lines. An interface equilibrium line exists in the area of the other stable phase representing metastable equilibrium of detectable phases.

(2) The phase diagram lines for the interphase equilibria represent lines of zero nucleation rates for the phases in equilibrium.

(3) The highest nucleation rate for a given constant pressure or temperature is obtained at the spinodal.

All of these assumptions are used to describe first-order phase transitions. In contrast, critical conditions are conditions for second-order phase transitions, where it is not possible for two or more phases to coexist. The main condition for nucleation is the ability to separate the initially homogeneous parent phase into two or more phases. This condition is contradictory to those of a second-order phase transition. Thus, the nucleation rate decreases when approaching a second-order phase transition and is equal to zero when the conditions of the second-order phase transition are attained. Since systems cannot reach the conditions of the second-order phase transition because of the growing fluctuations near the phase transition, it is only possible to discuss the phase transition limit.

To illustrate the main concepts of the semiempirical method to construct nucleation rate surfaces, a simple binary vapor system as originally presented by Anisimov et al.<sup>2</sup> will be briefly reviewed. An ideal binary solution with infinite solubility of components provides the simplest  $P$ – $X$  diagram at a constant temperature,  $T$  (Figure 2a). A cigar-like phase diagram (contour  $nfmn$ ) is obtained in this case. The nucleation rates,  $J$ , of the individual vapors are illustrated schematically by lines  $mh$  and  $ngd$ . Following the second assumption, the state diagram line  $nfm$  for the interface equilibria is a zero nucleation rate line. Line  $ab$  represents the spinodal conditions. The highest nucleation rate (third assumption) for isothermal condition is shown by line  $deh$ , over spinodal,  $ab$ . The gray surface of nucleation rates is depicted in this case within contour  $nfmhedgn$ . The nucleation rate curve for the initial composition  $X_0$  is represented schematically by line  $fe$ . The nucleation rate grows from zero, at point  $f$ , to a maximum at point  $e$ . The phase diagram provides the composition,  $X_1$ , of the initial critical embryo by using the lever relationship (through point  $r$ ). The resulting embryo composition at the spinodal condition should equal  $X_0$  because of the direct conversion of the parent phases since there is no barrier to nucleation. Curve  $gf$  reflects nucleation at a constant total pressure. The variation in the composition of the critical embryos can be seen as the second component varies from  $X = 0$  and  $X_1$ .

For the case of a nucleation temperature within the range spanned by the critical temperatures of the individual compo-

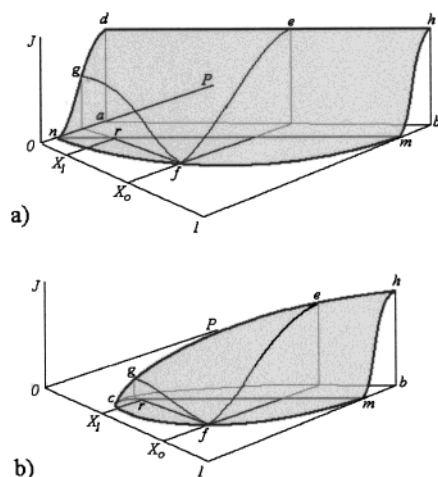


**Figure 2.** (a, b) Surface of the nucleation rate,  $J$ , for ideal binary mixture.  $X$  is the composition;  $P$  is the total pressure;  $ab$  (a) and  $cb$  (b) are spinodals;  $n, m$  are equilibrium pressures of individual components at temperature  $T$ ;  $fe$  is the nucleation rate for composition  $X_0$ ;  $gf$  is the isobaric nucleation rate; and  $c$  (b) is the critical point.

nents, the cigar-like diagram is transformed to a rounder shape, as shown schematically by contour  $mrcfn$  in Figure 2b, where point  $c$  is the critical point. In this case, a nucleation rate curve, such as  $mh$ , can be drawn for only one pure component. The equilibrium line  $cfm$  corresponds to a zero nucleation rate. The highest nucleation rate curve  $hegc$  is shown over the spinodal line,  $bc$ . The nucleation rate surface is colored gray. As in Figure 1a, the nucleation rates for a constant composition  $X_0$  of parent phase can be represented by line  $fe$  and isobaric nucleation by curve  $gf$ .

**Eutectic System.** In Figure 3a a phase diagram with a eutectic point is presented. The phase equilibrium lines obey the first assumption. The lines of the  $L_1 + V$  or  $L_2 + V$  phase equilibria with vapor and condensate can be extended to the conditions of the other stable phase, where  $L_1$  and  $L_2$  are liquids and  $V$  is vapor. These lines produce two cigar-like areas for the stable and metastable two-phase equilibria. The gray lines delimit areas of metastable two-phase equilibria of liquid phases,  $L_1$ , or,  $L_2$ , and vapor,  $V$ . Phase transformations in the condensed phases can be ignored. Then only the vapor-related parts of the diagram needs to be shown as presented in Figure 3b. The topology of the nucleation rate surfaces related to Figure 3b is represented in Figure 4. For each cigar in Figure 3b, the nucleation surface topology is similar to that presented in Figure 2a. The description of the light gray surface is the same as for Figure 2a. The letters with apostrophes define the dark gray surface and have meanings analogous to those of the letters for the light gray surface without apostrophes. These two nucleation rate surfaces illustrate the case of two independent nucleation channels. The resulting nucleation rate is the sum of the rates in each nucleation channel. Obviously, for single component nucleation, the nucleation rate for the other component should be zero. Thus, the total nucleation rate  $J_{\text{tot}}$  can be written as

$$J_{\text{tot}} = J_a(1 - X) + J_bX \quad (1)$$

where  $J_a$  and  $J_b$  are nucleation rates of individual components. The validity of this equation needs to be tested since the linearly additive relationship for nucleation rates are not obvious. The lever rule described by Anisimov et al.<sup>2</sup> holds only for the next nucleation stage; i.e., it could be applied to phase separation in the condensate.

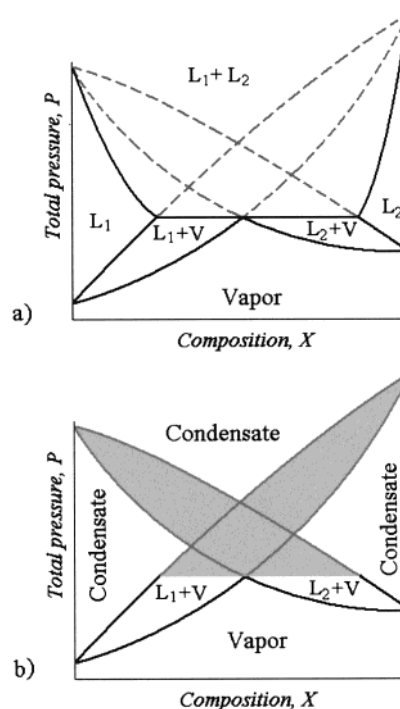


**Figure 3.** (a, b) Diagram for phase equilibria for case of partially miscible condensate (solid lines). Dotted lines represent the metastable vapor–liquid equilibria.  $L_1, L_2$  are two partially miscible liquids;  $V$  is vapor. The partial diagram (b) represents only vapor–liquid equilibria, where gray areas represent the metastable two-phase vapor–liquid equilibria.

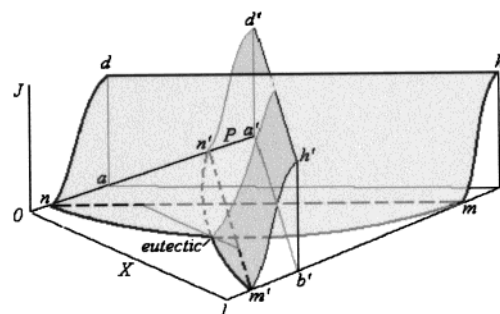


**Figure 4.** Schematic surfaces over the eutectic diagram representing two-canal nucleation. Nucleation rates equal to zero (not depicted in Figure) for the light gray diagram at pressure designated by point  $b$  and for the dark gray diagram at pressure designated by point  $a'$ . In the linear approximation the total nucleation rate through the canals,  $J_{\text{tot}}$ , could be written as  $J_{\text{tot}} = J_a(1 - X) + J_bX$ .

For the full representation of the nucleation rate,  $J$ , versus vapor activities,  $a_i$ , where the subscript  $i = 1, 2, \dots, n$  refers to the individual components, only limited information is available. Experimental results can be obtained for nucleation in binary systems. Adding limited experimental nucleation data can extend the equilibrium phase diagram. As assumed by Anisimov et al.,<sup>2</sup> the phase equilibrium lines represent zero nucleation rates. Such data are now available. Unfortunately, experimental nucleation results do not always have the corresponding measured equilibrium phase diagram available. There are a few systems where nucleation rates are found in the range from  $10^{-4}$  to  $10^{12} \text{ cm}^{-3} \text{ s}^{-1}$ . More often only experimental nucleation rate results are available only over a range of 2–5 orders of magnitude.

Prior to the 1980s, only critical vapor supersaturations were accurately measured. The first measurements of nucleation rate surfaces for binary systems were made by Anisimov et al.<sup>5</sup> and by Strej-Wagner.<sup>6</sup> These authors presented measurements of



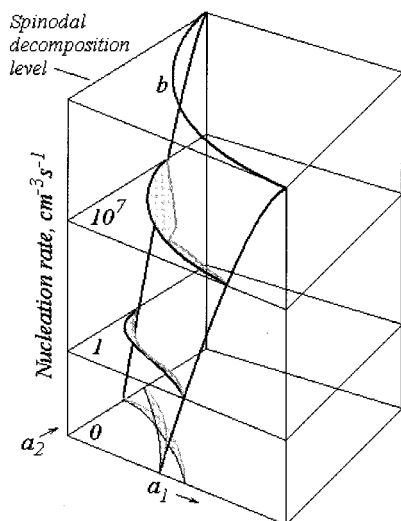


**Figure 5.** Schematic (not in a scale) representation of dynamic state phase diagrams<sup>4</sup> in the experimental axes: nucleation rate,  $J$ ; vapor activities  $a_i$ ,  $i = 1, 2$ .

binary, partially miscible components with variations in rates over 4 orders of magnitude. Commonly, the surface or surface sections for binary nucleation rates,  $J$ , are presented as a function of vapor activities  $a_1$  and  $a_2$ . Now one can construct a nucleation rate surface involving experimental nucleation rates and the phase diagrams. The schematic nucleation rate surface from zero nucleation rate to its upper limit at spinodal decomposition is presented by Anisimov et al.<sup>4</sup> These authors considered constant levels of nucleation rate as a type of “phase diagram”, that they termed dynamic state phase diagrams.<sup>4</sup> Using available experimental data, dynamic state phase diagrams were plotted for the water-*n*-propanol system. The highest nucleation rate was reconstructed using the trend of the experimental data. The corresponding nucleation rate surface has been redrawn from  $JXP$  to  $Ja_1a_2$  space. A schematic plot (Figure 5) presents the different levels of nucleation rates (not to scale). All isorates are taken from experiment except reconstructed line  $b$  for the spinodal nucleation. It can be seen that, at least for low nucleation rates, two surfaces of nucleation rate as in Figure 3 could be measured for appropriate compositions in the water-*n*-propanol system.

## Experimental Methods

Sulfur hexafluoride-*n*-pentanol nucleation was experimentally studied using a flow diffusion chamber (FDC). The *n*-pentanol used was from the single production lot distributed for use in all of the experiments resulting from the International Nucleation Workshop.<sup>7</sup> Sulfur hexafluoride,  $\text{SF}_6$  (Novosibirsk, Russia 99.95%) was used as the carrier gas.

The experimental device has been described in detail elsewhere.<sup>8,9</sup> Thus, only the basic principles of the FDC operation are given here. Filtered pure carrier gas is passed from the high-pressure cylinder to the vapor saturator (Figure 6). The saturator is filled with an inert chromatographic stationary phase (INZ-600; grain 0.25–0.5 mm) into which the substance of interest (about 20 wt %) is added. As sulfur hexafluoride passes through the stationary phase, it becomes fully saturated with *n*-pentanol vapor at the given total pressure and saturator temperature. The vapor saturator is continued to a laminator to force the development of laminar flow. Then the vapor-gas mixture enters the condenser (cooler) where it becomes supersaturated and nucleation can occur.

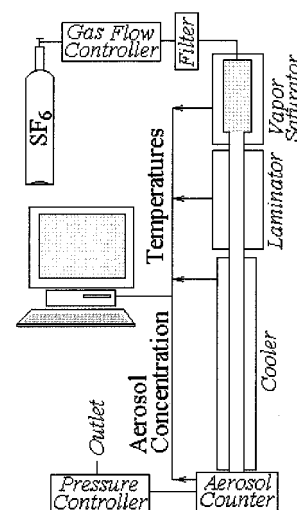


**Figure 6.** Flow diffusion chamber scheme. As sulfur hexafluoride passes through the saturator, it becomes saturated with *n*-pentanol vapor. The vapor-gas mixture enters to the cooler where nucleation occurs. Aerosol counter sensitivity was sufficient to detect every particle with a diameter greater than 0.1  $\mu\text{m}$ . All of the sensors' signals were digitized and stored in buffer memory and then passed to a personal computer for processing.

A laser photoelectric aerosol counter measured the concentration of particles. The counter sensitivity was sufficient to detect every particle with a diameter greater than 0.1  $\mu\text{m}$ . Temperatures were measured using copper-constantan thermocouples that were calibrated over the appropriate temperature range using mercury thermometers with an accuracy of 0.1  $^\circ\text{C}$ . A laminar flow regime was ensured inside the aerosol generator by using a low volumetric flow rate,  $Q = 6.0 \text{ cm}^3/\text{s}$ . This flow yields a Reynolds number about 100. The total pressure in the generator and aerosol counter were the same and constant for each experimental series. The total pressure was varied from set to set within the total pressure interval of 0.10–0.30 MPa with steps of 0.1 MPa. The standard deviations of the measured aerosol concentrations did not exceed 3% in these experiments. All of the sensors' signals were digitized and stored in buffer memory and then passed to a personal computer for further processing.

To estimate the experimental vapor supersaturation ratio,  $S$ , the nucleation temperature and the partial vapor pressure,  $P_{v,\text{exp}}$ , of *n*-pentanol must be known. Vapor supersaturation is calculated as

$$S = \frac{P_{v,\text{exp}}}{P_{\text{sat},\text{exp}}} = \frac{P_{\text{tot}}x_v}{P_{\text{sat},\text{exp}}} \quad (2)$$

where  $x_v$  is the *n*-pentanol vapor mole fraction in the vapor-gas mixture,  $P_{\text{sat}}$  and  $P_{\text{tot}}$  are saturated vapor pressure and total pressure, respectively; the subscript exp refers to the experimental values. The maximum rate of aerosol particle formation was calculated in the same fashion as described by Anisimov et al.<sup>8</sup>

$$J_{\text{exp}}^{\text{max}} = \frac{N_{\text{exp}}J_{\text{theor}}^{\text{max}}}{\int J_{\text{theor}} dv} \quad (3)$$

where  $N_{\text{exp}}$  and  $\int J_{\text{theor}} dv$  are the experimental and theoretical numbers of particles, respectively, produced by the system per unit time;  $J_{\text{theor}}^{\text{max}}$  is the maximum of the theoretical nucleation rate in the experimental device. In the experiment, the particle

**TABLE 1: Thermophysical Properties of Sulfur Hexafluoride, SF<sub>6</sub>, *n*-Pentanol, and Their Mixture<sup>a</sup>**

Sulfur Hexafluoride	
$m_1 = 146.05 \times 10^{-3} \text{ kg/mol}$ , $\sigma_1 = 5.128 \times 10^{-10} \text{ m}$ , $\epsilon_1/k_B = 222.1 \text{ K}$ (ref 27)	
$\lambda_1 = T^{1.75}(5.465 \times 10^{-7} - 1.345 \times 10^{-8}P) + 4.605 \times 10^{-4}P + 9.131 \times 10^{-4} \text{ J m}^{-1} \text{ s}^{-1} \text{ K}^{-1}$ (ref 12)	
$(P \text{ is expressed in physical atmospheres})$	
$\mu_1 = 5/16(\pi m_1 R_g T)^{1/2}/N_A/\pi/\sigma_1^2/\Omega_{22}(k_B T/\epsilon_1)$ (ref 14)	
$C_{P1} = 4R_g/m_1$	
<i>n</i> -Pentanol <sup>15</sup>	
$m_2 = 88.150 \times 10^{-3} \text{ kg mol}^{-1}$ (ref 27), $\sigma_2 = 6.667 \times 10^{-10} \text{ m}$ , $\epsilon_2/k_B = 304.1 \text{ K}$ (ref 15)	
$\lambda_2 = 1.88 \times 10^{-2} - 9.068 \times 10^{-5}T + 2.456 \times 10^{-7}T^2 \text{ J m}^{-1} \text{ s}^{-1} \text{ K}^{-1}$	
$C_{P2} = (3.8686 + 0.50451T - 2.6394 \times 10^{-4}T^2 + 5.12 \times 10^{-8}T^3)/m_2$	
$\rho_1 = 270 + 10^3(1.930229Z^{1/3} - 8.414762Z^{2/3} + 19.226001Z - 18.559303Z^{4/3} + 6.555718Z^{5/3})$	
$(Z = 1 - T/588.15)$	
$\gamma_2 = (26.85469 - 0.07889(T - 273.16)) \times 10^{-3} \text{ N m}^{-1}$	
$P_{\text{sat}} = 133.322 \exp(90.079 - 9788.3/T - 9.9000 \ln T) \text{ Pa}$ (ref 10)	
Sulfur Hexafluoride and <i>n</i> -Pentanol Mixture	
$\sigma_{12} = (\sigma_1 + \sigma_2)/2$ , $\epsilon_{12} = (\epsilon_1\epsilon_2)^{1/2}$ , $C_P = (1 - c)C_{P1} + cC_{P2}$ , $\alpha = 0$	
$\rho D_{12} = 3m_1[R_g T(m_1 + m_2)/(2\pi m_1 m_2)]^{1/2}/(8N_A\sigma_{12}^2\Omega^{(1,1)}(T_{12}^*))$ (ref 14)	
$\mu = \mu_1 c_1/[c_1 + c_2\Phi_{12}M_1/M_2] + c_2\mu_2/[c_2 + c_1\Phi_{12}M_2/M_1]$ (ref 13)	
$\Phi_{ij} = \{[1 + (\mu_i/\mu_j)^{1/2}(M_j/M_i)^{1/4}]^2/\{[8(1 + M_i/M_j)]^{1/2}\}\}$	
$\lambda = \lambda_1(1 - c)(1 - c + cA_{12}m_1/m_2)^{-1} + \lambda_2 c(c + (1 - c)A_{21}m_2/m_1)^{-1}$ (ref 13)	
$A_{nm} = [1 + (\lambda_{nm}/\lambda_{im})^{1/2}(m_n/m_m)^{1/4}]^2/[8(1 + m_n/m_m)]^{-1/2}$	
$\lambda_{im}/\lambda_{nm} = (m_m^{1/2}\sigma_m^2\Omega^{(2,2)}(T_{nm}^*))/(m_n^{1/2}\sigma_n^2\Omega^{(2,2)}(T_{nm}^*))$ , $n, m = 1, 2$	
$\Omega^{(i,j)}(T_{nm}^*) = A_{ij}/(T_{nm}^*)^{B_{ij}} + C_{ij}/\exp(D_{ij}T_{nm}^*) + E_{ij}/\exp(F_{ij}T_{nm}^*) + G_{ij}/\exp(H_{ij}T_{nm}^*)$ (ref 13)	
$T_{nm}^* = (k_B T/\epsilon_{nm}) \in [0.3; 100]$	
$A_{11} = 1.06036$ , $B_{11} = 0.15610$ , $C_{11} = 0.19300$ , $D_{11} = 0.47635$	
$E_{11} = 1.03587$ , $F_{11} = 1.52996$ , $G_{11} = 1.76474$ , $H_{11} = 3.89411$ , $A_{22} = 1.16145$ , $B_{22} = 0.14874$	
$C_{22} = 0.52487$ , $D_{22} = 0.77320$ , $E_{22} = 2.16178$ , $F_{22} = 2.43787$ , $G_{22} = H_{22} = 0$	

<sup>a</sup> Indices 1 and 2 refer to sulfur hexafluoride and *n*-pentanol, respectively, and index 12 and no index refer to their mixture;  $m$  is molar mass (kg/mol),  $\lambda$  is thermal conductivity ( $\text{J m}^{-1} \text{ s}^{-1} \text{ K}^{-1}$ ),  $\mu$  is viscosity,  $\sigma$  and  $\epsilon_1$  are parameters of Lennard-Jones interactions,  $\Omega$  is collision's integral,  $N_A$  and  $k_B$  are Avogadro's and Boltzmann's constants,  $R_g$  is the gas universal constant,  $C_P$  is specific heat capacity at constant pressure ( $\text{J kg}^{-1} \text{ K}^{-1}$ ),  $\gamma$  is surface tension ( $\text{N m}^{-1}$ ),  $P_{\text{sat}}$  is vapor saturation pressure (Pa),  $\rho$  is density ( $\text{kg/m}^3$ ),  $D_{12}$  is binary diffusion factor ( $\text{m}^2/\text{s}$ ), and  $\alpha$  is thermodiffusion factor.

concentration,  $C_{\text{exp}}$ , is measured.  $C_{\text{exp}} = N_{\text{exp}}/Q$ , where  $N_{\text{exp}}$ , as mentioned above, is numbers of particles, produced by the aerosol generator per unit time and  $Q$  is a volumetric rate of gas flow. The theoretical nucleation rate was calculated using the classical nucleation theory. The theoretical inconsistencies are largely canceled out by the ratio of theoretical values in eq 2. The correlation used for the saturated vapor pressure,  $P_{\text{sat}}$ , was given by Schmeling and Strey<sup>10</sup> and is presented in Table 1.

The temperature and *n*-pentanol vapor concentration distributions inside the condenser were evaluated by solving the heat and mass transfer problem for a steady-state laminar viscous vapor–gas flow with axial symmetry. The set of Navier–Stokes equations has been solved in the approximation of a long channel. Vapor boundary conditions for the *n*-pentanol were chosen to be similar to those recently employed for the static diffusion chamber.<sup>11</sup> The thermophysical properties of sulfur hexafluoride, *n*-pentanol, and their mixtures<sup>12–15</sup> are presented in Table 1.

## Experimental Results and Discussion

The experimental results for *n*-pentanol–sulfur hexafluoride for total pressures 0.10, 0.20, and 0.30 MPa are presented in Figure 7. All experimental conditions were recalculated to a nucleation temperature of 255.0 K.

The experiments were conducted at quasisteady-state conditions with the saturation temperature increasing at a rate of 0.2–0.6 deg/min. The condenser temperature was constant for all experiments. One can see the truly remarkable shape of nucleation rate curves. The nucleation seeds level provides heterogeneous nucleation at rates of the order of  $2\text{--}3 \text{ cm}^{-3} \text{ s}^{-1}$ . The first impression of these results was that shape is caused by the depletion of the sample liquid from the vapor saturator.

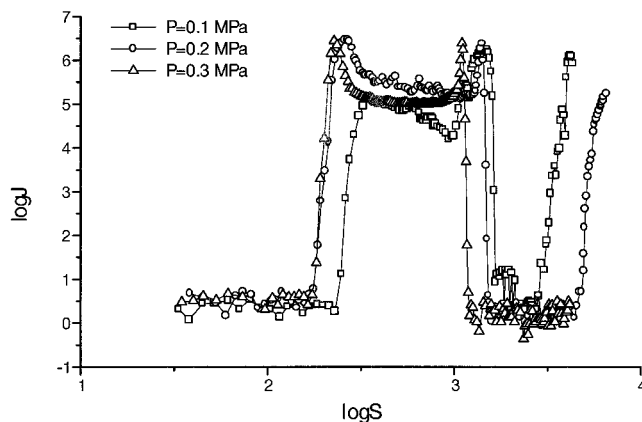


**Figure 7.** *n*-Pentanol–sulfur hexafluoride nucleation rates at total pressures 0.10, 0.20, and 0.30 MPa and nucleation temperature 255 K.

The saturator was reloaded several times with the *n*-pentanol, and the experiment was repeated for the conditions leading to the plateau between  $\log S = 2.3$  and  $3.1$ . The two peaks limiting the plateau were surprising but reproducible. The nucleation rate collapse beyond  $\log S = 3.1$  and its next rise near  $\log S = 3.5$  were also repeatable. With increasing pressure, changes in nucleation rate can be observed. In particular, the last peak shifts from  $\log S = 3.5$  to higher values and reached the limit of available vapor saturation for the given experimental system.

Together with the previous result by Anisimova et al.,<sup>3</sup> the present result illustrates the experimental evidence of multiple nucleation rate surfaces originally discussed by Anisimov et al.<sup>2</sup> We suggest that multiple nucleation rate surfaces can be found in other nucleation studies. Preliminary results for *n*-pentanol–sulfur hexafluoride nucleation were obtained in 1996. The result was so unusual that it remained unreported until there was

clearer evidence for multiple nucleation rate surfaces. A special experiment needs to be developed similar to those done by Anisimova et al.<sup>3</sup> to detect the two independent nucleation rate surfaces for the topology in the neighborhood of the triple point. Without further information, it is difficult to fully understand these results in the context of a complex nucleation rate surface, but we believe that these results are evidence of the existence of multiple nucleation surfaces with a not yet fully defined topology. The simplified topology presented in Figure 4 provides an adequate reflection of the two-peak plateau, but to obtain the next nucleation rate rise, the phase diagram should have more elements than a simple diagram with a eutectic point. The semiempirical construction of the nucleation rate surfaces can be helpful equally with other pure theoretical methods to improve our understanding of nucleation phenomena.

## Conclusions

The multiple measurements of the *n*-pentanol–helium system<sup>7</sup> are very important to obtain vapor nucleation rates independent of specific experimental methodologies and variability. The semiempirical approximation embodied in eq 6 of Anisimov et al.<sup>16</sup> can be used as a basis of comparison in nucleation rate studies because it provides a scale for the comparison of various nucleation rate measurements at different nucleation temperature from different research groups. Consistent results for nucleation at various pressures from different groups are needed because different research groups have interpreted pressure effects differently.

The idea of semiempirical construction of nucleation rates surfaces by Anisimov et al.<sup>2</sup> indicates conditions where the multiple nucleation rate surface can be detected. Experiments using particle size measurements can be performed to detect two independent nucleation rate surfaces. For example, Anisimova et al.<sup>3</sup> used such measurements to explore the dynamics of particle formation through two independent nucleation channels representing two separate nucleation rate surfaces. Another example of the presence of multiple nucleation rate surfaces is found in the example of *n*-pentanol–sulfur hexafluoride nucleation. To fully explain the details of *n*-pentanol–sulfur hexafluoride nucleation, it will be necessary to have the phase diagram for this system.

Vapor–gas nucleation in most cases is a binary system with partial solubility of the components. The topology of the nucleation rate surface in this case is close to the topology presented in Figure 4. It leads to the conclusion that the multiple nucleation rate surfaces can be found in many other systems under investigation.

**Acknowledgment.** We gratefully acknowledge Prof. Howard Reiss, whose more than 50 years of scientific activities is being

celebrated by the aerosol community, for support of our idea of semiempirical construction of the nucleation rate surfaces over the phase states diagrams. Dr. R. Strey is acknowledged for providing the *n*-pentanol sample from one lot (Merck *n*-pentanol, Lot No. K21223075518) within the scope of joint experiments by the International Nucleation Workshop Group. Dr. V. Kosjakov, who attracted the author's attention that the previous formulation of lever rule<sup>2</sup> could be developed for metastable phases, as well as Dr. S. Shandakov and Dr. V. Pinaev, who helped us on different stages of this research, are acknowledged. The work at Clarkson University was supported by the National Science Foundation under Grant No. CTS 9976615.

## References and Notes

- (1) Senger, B.; Shaaf, P.; Corti, D. S.; Bowles, R.; Voegel, J.-C.; Reiss, H. *J. Chem. Phys.* **1999**, *110*, 6421. Senger, B.; Shaaf, P.; Corti, D. S.; Bowles, R.; Pointu, D.; Voegel, J.-C.; Reiss, H. *J. Chem. Phys.* **1999**, *110*, 6438.
- (2) Anisimov, M. P.; Hopke, P. K.; Rasmussen, D. H.; Shandakov, S. D.; Pinaev, V. A. *J. Chem. Phys.* **1998**, *109*, 1435.
- (3) Anisimova, L.; Hopke, P. K.; Terry, J. *J. Chem. Phys.* **2001**, *114*, 9852.
- (4) Anisimov, M. P.; Shandakov, S. D.; Pinaev, V.; Shvets, I.; Hopke, P. K. Dynamic State Phase Diagrams For Nucleated Systems. In *Nucleation and Atmospheric Aerosols 2000*; Hale, Barbara N., Kulmala, Markku, Eds.; IAP: Melville, NY, 2000; pp 315–318.
- (5) Anisimov, M. P.; Vershinin, S. N. Spontaneous nucleation rate, size and composition of critical embryos in many components supersaturated vapor. In *Lecture Notes in Physics*; 1988; No. 309, p 393. Experimental results for the glycerin–dibutylphthalate nucleation in space nucleation rate, *J*, and vapor activities ( $S_{C_3H_8O_3}$  and  $S_{C_{10}H_{12}O_4}$ ) of components were published for the first time by: Anisimov, M. P. *Preprint INH SOAN*; Institute of Inorganic Chemistry SBAS USSR: Novosibirsk, 1981; No. 12, 24 pp.
- (6) Strey, R.; Wagner, P. E. Measurements of the heteromolecular homogeneous nucleation of partially miscible liquids. In *Lecture Notes in Physics*; 1988; No. 309, p 371.
- (7) Smolik, J.; Wagner, P. E. In *Nucleation and Atmospheric Aerosols*; Kulmala, M., Wagner, P. E., Eds.; Pergamon: Helsinki, Finland, 1996; p 58.
- (8) Anisimov, M. P.; Koropchak, J. A.; Nasibulin, A. G.; Timoshina, L. V. *J. Chem. Phys.* **1998**, *109* (22), 10004.
- (9) Anisimov, M. P.; Koropchak, J. A.; Nasibulin, A. G.; Timoshina, L. V. *J. Chem. Phys.* **1998**, *112* (22), 9917.
- (10) Schmeling, T.; Strey, R. *Ber Bunsen-Ges. Chem. Phys.* **1983**, *87*, 871.
- (11) Anisimov, M. P.; Shandakov, S. D.; Polygalov, Yu. I.; Heist, R. H. *J. Chem. Phys.* **2001**, *114* (2), 899.
- (12) Vargaftic, N. B.; Fillipov, L. P.; Tarzimanov, A. A. Totiskii, E. E. *Handbook on Thermal Conductivity of Liquids and Gases*; Energoatomizdat: Moscow, 1990.
- (13) Rid, R. C.; Prausnitz, J. M.; Sherwood, Th. K. *The Properties of Gases and Liquids*; McGraw-Hill: New York, 1971.
- (14) Hirschfelder, J. O.; Curtiss, C. F.; Bird, R. B. *Molecular Theory of Gases and Liquids*; Wiley: New York, 1954.
- (15) Rudek, M.; Katz, J. L.; Vidensky, I. Y.; Zdimal, V.; Smolik, J. *J. Chem. Phys.* **1999**, *111* (8), 3623.
- (16) Anisimov, M. P.; Hopke, P. K.; Shandakov, S. D.; Shvets, I. *J. Chem. Phys.* **2000**, *113* (5), 1971.